

An Unified AMBER-Compatible Molecular Mechanics Force Field for Thiolate Protected Gold Nanoclusters

*

E-mail:

Abstract

*To whom correspondence should be addressed

Introduction

Thiolate-protected Gold nanoclusters $\text{Au}_n(\text{SR})_m$ have been extensively studied during the past years, both experimentally and theoretically.¹ Clusters studied so far range in size and nature of the ligand and exhibit interesting electronic, optical, or catalytic properties that could make them promising building blocks for nanotechnology applications. Because the ligand R-group can easily be made bio-compatible, these thiolate protected clusters are also increasingly used in biological research. For example, the clusters have been conjugated with biomolecules to act as contrast agents in electron microscopy imaging, or as molecular rulers.

Whereas density functional theory (DFT) has been widely used to investigate the electronic, optical and even catalytic properties of gold nanoclusters, the system size and timescales that must be reached to investigate the interactions between gold clusters and biomolecules precludes DFT and necessitates classical molecular dynamics simulation in combination with a molecular mechanics force field instead. To date, several molecular dynamics simulations have been performed on systems containing gold, either as a surface or a nanoparticle. However, as most of these studies were focussed on a specific gold cluster, the force field parameters are often not transferrable to clusters with different sizes or ligands.

A notable exception are reactive force fields for gold nanoparticles, such as REAXFF, which is readily transferred between clusters. However, due to the high complexity of the potential functions, the large number of parameters and lack of compatibility with the available biomolecular force fields, reactive force fields are not yet available in mainstream molecular dynamics programs. Moreover, the small time step with which the equations of motions have to be integrated in reactive force field simulations creates a severe bottleneck for simulating large biological systems. Alternatively, the QM/MM approach, in which the gold cluster is described at the QM level, is transferrable as well, but the computational effort required for the QM calculation restricts accessing the biologically relevant timescales

in the simulation.

To systematically investigate the effect of size and composition of thio-protected gold clusters on their interplay with biomolecules, such as proteins, membranes, or nucleic acids, we need a transferrable force field that is compatible with an existing biomolecular force field. Since the AMBER force field has been specifically developed for a wide range of biomolecules, we have optimized a set of generic parameters to model the energetics of thiolate-protected gold clusters with the AMBER potential functions. To facilitate transferrability, we avoided bonding interactions between gold atoms in the core, and rely on non-covalent interaction between gold atoms instead to maintain the core structure. To verify the validity of the new force field, we have performed MD simulations on five representative thio-protected gold nanoclusters (Figure 1) and compared the results of these simulations to the available experimental data and DFT computations.

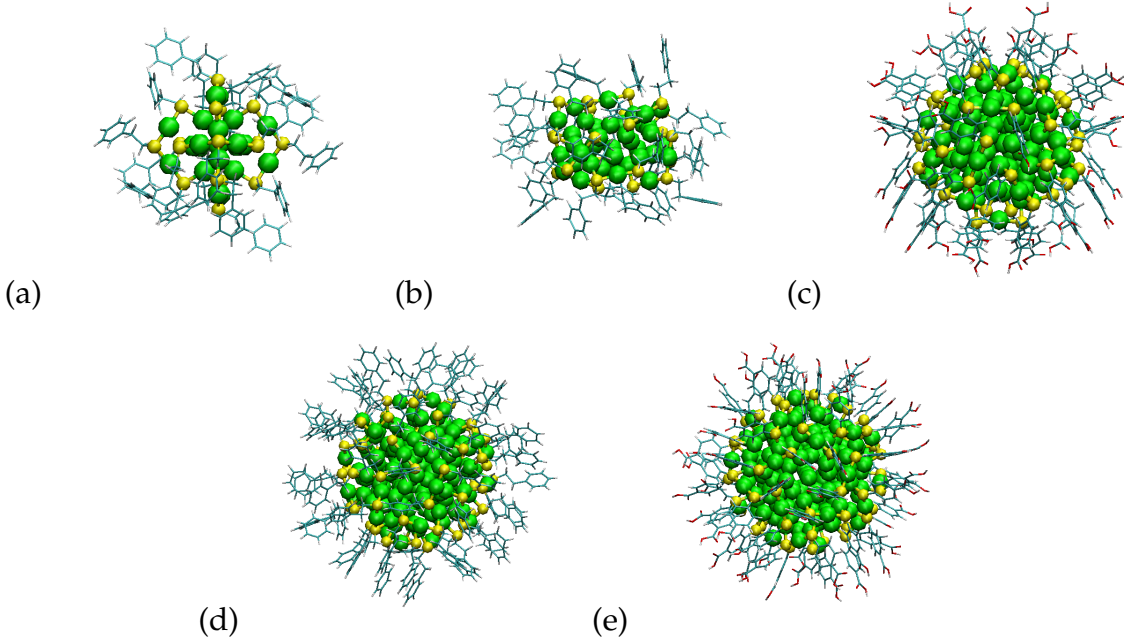


Figure 1: Clusters studied in this work. Coloring convention: green=gold; yellow=sulfur; cyan=carbon; white=hydrogen; red=oxygen. (a) $\text{Au}_{25}(\text{PET})_{18}^-$ (b) $\text{Au}_{38}(\text{PET})_{24}$ (c) $\text{Au}_{102}(\text{pMBA})_{44}$ (d) $\text{Au}_{144}(\text{PET})_{60}$ (e) $\text{Au}_{144}(\text{pMBA})_{60}$

Methods

In this work we derive a general force field for thiolate protected gold nanoclusters based on a representative set of five clusters (Figure 1). The geometries of these clusters were taken from the literature: $\text{Au}_{25}(\text{PET})_{18}$ from ref, $\text{Au}_{38}(\text{PET})_{24}$ from, $\text{Au}_{102}(\text{pMBA})_{44}$, $\text{Au}_{144}(\text{PET})_{60}$ from⁷ and $\text{Au}_{144}(\text{pMBA})_{60}$ from. All MD simulations were performed with Gromacs, versions 4.5 and 4.6.

Parameterization

The shape and anatomy of a gold cluster is controlled by the number of gold atoms, the chemical nature of the ligands and the number of these ligands. The core consists of gold atoms arranged in shells. This arrangement depends on the number of gold atoms. For example, Au_{25} cluster has one gold atom in the center around which twelve gold atoms form an icosahedron. In Au_{38} the core is less symmetric and is composed of two merged icosahedra. Larger clusters, such as Au_{102} and Au_{144} , contain more gold layers with icosahedral center and a more globular overall shape.

In previous force fields, constraints were employed to fix the distances between the gold atoms of the core and maintain its geometry. Such approach, however, requires knowledge about the interatomic distances, which vary with cluster size. Therefore, force field based on constraints between the core atoms are not transferrable and cannot be used to predict the geometry of new gold clusters.

Instead, transferrability requires that the force field functions and parameters for the gold core do not depend on the details of the cluster. To fulfill that requirement, we used the non-covalent Lennard-Jones interatomic potential with parameters for metallic gold, as in ref. In addition, no partial charges are assigned to the gold atoms in the core. Although this choice was obviously motivated by our requirement that the force field parameters are transferrable to other clusters, it was justified by Bader analyses on a various thio-protected

gold nanoclusters, which suggest that the core atoms are indeed almost neutral in most clusters.

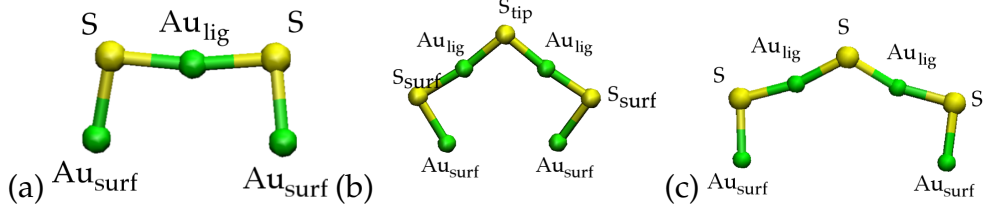


Figure 2: Different ligand unit formations related to clusters studied in this work with naming conventions and colors gold (green) and sulfur (yellow) . (a) Shows the rectangular staple formation present in Au_{38} , Au_{102} and Au_{144} clusters. The V-shape staple formation in (b) appears in Au_{25} and Au_{38} clusters and (c) in Au_{102} cluster (together with (a)). The alkylthiol groups are omitted.

The core is separated from the ligands by a sulfur-gold interface layer that protects the core. The sulfur atoms connect the ligands to the core by forming so-called staples (figure 2, in which the thiolates bind covalently with one gold atom at the surface (Au_{surf} , green) and another at the interface (Au_{lig} , Figure 2). To describe these covalent interactions with a minimal set of parameters, valid for a wide range of gold clusters, the equilibrium bond lengths and angles were defined as the average of these values in the DFT optimized structures of the five clusters, shown in Figure 1. However, due to the large variation of the $\text{Au}_{\text{lig}}-\text{S}_{\text{tip}}-\text{Au}_{\text{lig}}$ in the V-shaped stables between the smaller (100° in $\text{Au}_{25}(\text{PET})_{18}$ and $\text{Au}_{38}(\text{PET})_{18}$) and larger clusters (119.2° in $\text{Au}_{102}(\text{PET})_{44}$, figure 2), the equilibrium value of this angle had to be made cluster-specific. The harmonic force constant for the Au_x-S bonds was adopted from². This force constant is approximately an order of magnitude smaller than the usual angle force constants in AMBER. The harmonic force constants for the $\text{Au}_x-\text{S}-\text{Au}_x$ angles were taken from reference³, which are comparable to those in AMBER. The force constant for the $\text{S}-\text{Au}_{\text{lig}}-\text{S}$ angle was also taken from reference³. This force constant is about three times larger than the typical angle force constants in AMBER, but is essential to maintain the strained staple shape. For angles involving gold and ligand atoms ($\text{Au}_x-\text{S}-\text{C}_x$) we used the same force constants as Banerjee *et al.*², which

are somewhat smaller than those in AMBER.

Finally, the ligand layer consist of typical organic molecules that contain atom types for which AMBER parameters are already available. However, for some combinations of these atoms, bonded or angle parameters were missing. Missing equilibrium values were determined by averaging these values over the DFT optimized structures, while missing force constants were selected based on similarity with existing interactions. The partial charges on the ligand atoms were optimized with Ambertools12,⁴ following the RESP charge fitting procedure recommended for AMBER.. Charges were derived for a model system consisting of two gold atoms connected to two ligands via a sulfur atom, *i.e.*: $\text{Au}_2(\text{PET})_2$ and $\text{Au}_2(\text{pMBA})_2$. Similar model systems have been used previously in gold-thiolate parameter derivations.^{2,5} The geometries of $\text{Au}_2(\text{PET})_2$ and $\text{Au}_2(\text{pMBA})_2$ were optimized using Gaussian09⁶, using the B3LYP functional in combination with LANL2DZ basis set and the W06 density fitting basis⁷. The electron density of the optimized structure was used to calculate the electrostatic potential on a grid of X points in Y concentric shells around the molecule. The radius of Au was set to 0.17 nm. Atomic charges were fitted to this potential in a two-stage RESP procedure, constraining the charges of Au to zero. For the pMBA ligand the partial charges were fitted for both protonated and deprotonated structures. For the non-neutral $\text{Au}_{25}\text{PET}_{18}^{(-)}$ cluster, the negative charge was distributed over all ligands by scaling all charges. The optimized charges were close to the default AMBER charges of similar residues. Although we only considered the pMBA and PET ligands (Figure 3), the procedure to parameterize the ligand is sufficiently general to be applied to other ligands as well. Therefore, parameters for new ligands can be easily obtained without modifying any of the core or interface parameters.

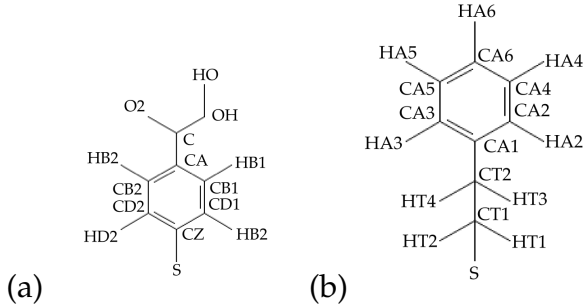


Figure 3: Alkylthiol ligands and naming conventions used in this work (a) pMBA= para-mercaptopbenzoic acid and (b) PET= phenyl-ethanethiol.

Force field validation

Molecular dynamics simulations

The new force field was tested by performing 100 ns MD simulations of the five clusters in solvent. In all simulations, the leap-frog Verlet integrator was used with time step of 2 fs, periodic boundary conditions, a 1.0 nm Lennard-Jones cut-off with dispersion correction for energy and pressure, PME electrostatics with a 1.0 nm cut-off and 0.12 nm grid spacing, the velocity-rescale thermostat with a reference temperature of 298.15 K and coupling time constant of 0.1 ps,⁷ and the Berendsen barostat with a reference pressure of 1 bar and coupling time constant of 1 ps.⁷ All bond lengths were constrained with the LINCS algorithm.⁷ The Au₂₅(PET)₁₈ and Au₃₈(PET)₂₄ clusters were simulated in chloroform. Chloroform and dichloromethane (GAFF⁸) parameters and structures were obtained from Virtualchemistry website^{9,10}. Both neutral and anionic forms of the Au₂₅(PET)₁₈⁽⁻⁾ cluster were simulated. Clusters Au₁₀₂(pMBA)₄₄ and Au₁₄₄(pMBA)₆₀ were simulated in TIP3P water, with all pMBA groups deprotonated. Sodium and Chloride ions were added to neutralize the system at a concentration of 0.1 M. The Au₁₄₄(PET)₆₀ cluster was simulated in dichloromethane. Prior to the production simulations, each system was energy minimized and equilibrated under NVT (100 ps) and NPT (100 ps) conditions. The deprotonated Au₁₀₂(pMBA)₄₄ and Au₁₄₄(pMBA)₆₀ systems were equilibrated for 1 ns

under NPT conditions with a 1 fs timestep.

Density functional theory computations

DFT optimizations were performed with the real-space grid projector augmented wave code-package GPAW¹¹. Activation barriers for flipping the chirality of the sulfur atoms were computed for a model system containing a single staple with three thiolate ligands (PET or pMBA) and 4 gold atoms (Figure ??). The reaction coordinate was defined as the torsion angle between the Au₁-S₂ and S₃-C₄ bond vectors. This angle was varied in 23 and 18 discrete steps of 5.7° and 6.5° for the pMBA and PET model systems, respectively, followed by a constrained geometry optimization keeping both torsion angle and the two dangling gold atoms fixed. Afterwards, the potential energy profiles were re-evaluated at the force field level to verify the validity of the latter.

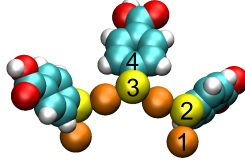


Figure 4: Model system and reaction coordinate for computing the energy profile for flipping the chirality of the central sulfur atoms. The reaction coordinate is defined as the torsion angle between the bond vectors Au₁-S₂ and S₃-C₄. For the rest of the ligand both PET and pMBA are used, but only pMBA is shown here.

Further validation based on DFT was performed by comparing structural fluctuations between force field and DFT MD simulations of Au₂₅PET₁₈⁻ and Au₂₅H₁₈⁻ at 300 K. The force field simulations were carried out in vacuum, without cut-offs for Lennard-Jones or electrostatic interactions, using a stochastic dynamics integrator with a 1 fs timestep, a reference temperature of 300 K and a friction coefficient of 0.01 ps⁻¹. Bonds involving hydrogen atoms were constrained. The classical DFT-based molecular dynamics simulations were performed with the LDA functional and the LCAO double zeta basis set using a Langevin integrator, with a friction of 0.004 ps⁻¹ and a 1 fs timestep. The Au₂₅PET₁₈⁻

cluster was thermalized slowly to 300 K and subsequently simulated for 0.5 ps, while the 10 ps molecular dynamics trajectory of $\text{Au}_{25}\text{H}_{18}^-$ was taken from previous work.¹²

Diffusion coefficients

Diffusion coefficients for free diffusion of $\text{Au}_{25}(\text{PET})_{18}$ and $\text{Au}_{38}(\text{PET})_{24}$ in chloroform and $\text{Au}_{144}(\text{PET})_{60}$ in dichloromethane were determined from 20 independent NPT simulations of 5 ns at 289.15 K and 1 bar. Initial conditions were generated by randomly assigning velocities from a Maxwell-Boltzmann distribution to the atoms of the starting structure that was created by placing the cluster in the center of a cubic periodic box filled with solvent. As before the force field parameters for the chloroform and dichloromethane solvents were obtained from VirtualChemistry.org. To account for finite size effects, the simulations were repeated with three different box sizes.⁷ Prior to the production runs, the simulation boxes were equilibrated for 2.1 ns.

Diffusion coefficients were calculated from the Einstein diffusion equation (in three dimensions):

$$D_{\text{cluster}} = \lim_{t \rightarrow \infty} \frac{\langle ||\mathbf{r}_i(t) - \mathbf{r}_i(0)||^2 \rangle}{6t} \quad (1)$$

where $\langle ||\mathbf{r}_i(t) - \mathbf{r}_i(0)||^2 \rangle$ denotes the mean square displacement (MSD). The Stokes-Einstein equation relates the hydrodynamic radius r of a spherical particle in homogeneous solution to its diffusion coefficient by

$$r = \frac{k_B T}{6\pi D_{\text{cluster}} \eta} \quad (2)$$

where η is the viscosity of the solvent.

Following Yeh and Hummer, we averaged the mean-square-displacements (MSDs) over the 20 independent 5 ns simulations for each cluster. The diffusion coefficient was obtained by linear fitting the MSD from 0.5 to 4.5 ns to equation ???. Errors were estimated from the difference between the fits from 0.5 to 2.5 ns and from 2.5 to 4.5 ns. As suggested

in reference¹³, an error-weighted linear fit was performed to the diffusion coefficients as a function of the inverse box length. The diffusion coefficient at infinite dilution was estimated from the intercept of this fit.

Crystal simulations

Further validation was performed by simulating a crystal of $\text{Au}_{102}(\text{pMBA})_{44}$ ¹⁴ under the experimental crystallization conditions and comparing the structural dynamics to the x-ray data. For this purpose a periodic unitcell with 72 neutral (protonated) $\text{Au}_{102}(\text{pMBA})_{44}$ clusters was created and solvated in a mixture of water/methanol/NaCl/NaOAc, which corresponds approximately to the crystallization conditions reported in experiment.. The water was described with the TIP3P model,, the methanol (GAFF) parameters were obtained from Virtualchemistry and sodium acetate was parameterized with Ambertools12, using the default settings. After energy minimization, the system was equilibrated for 1 ns at 200 K and fixed volume with position restraints on the heavy atoms of the clusters. After that, positions restraints were removed and the system was further equilibrated for 1 ns at 298.15 K and constant volume and subsequently for another ns at 298.15 K and 1 bar pressure. After these equilibration steps, the system was simulated for 100 ns at 298.15 K and 1 bar pressure. To investigate the influence of the crystallization liquid, we also performed a simulations with only TIP3P water.

Results and discussion

Parameters

Table 1 lists the AMBER atom types for thioprotected gold nanoclusters, Lennard-Jones parameters σ and ϵ and partial charges. The Lennard-Jones parameters for gold were obtained from ref.¹⁵, while all other atom types are standard types found in AMBER. Because the atom types determine the force constants and equilibrium values for bonded

interactions, we only report the bonded parameters that we have introduced ourselves (Table 2). These force constants and equilibrium values describe interactions that involve known atomtypes, but that were not yet included in the default AMBER force field.

Table 1: Non-bonded parameters for all atom types used in simulations. Partial charges for deprotonated pMBA, and PET ligand to obtain negatively charged $\text{Au}_{25}(\text{PET})_{18}^-$ cluster are presented in parentheses () .

| Atom name | Atom type | σ (nm) | ϵ (kJ/mol) | q (e) |
|-----------------|----------------|---------------|---------------------|-------------------|
| Au | Au | 0.2629 | 22.1330 | 0 |
| pMBA | | | | |
| C | C | 0.0339967 | 0.359824 | 0.6641 (0.7245) |
| CZ | CA | " " | " " | 0.0689 (0.0827) |
| CD ₁ | CA | " " | " " | -0.0557 (-0.0707) |
| CB ₁ | CA | " " | " " | -0.1604 (-0.1985) |
| CA | CA | " " | " " | -0.0029 (0.0463) |
| CB ₂ | CA | " " | " " | -0.1604 (-0.1985) |
| CD ₂ | CA | " " | " " | -0.0557 (-0.0707) |
| HD ₁ | HA | 0.259964 | 0.06276 | 0.1191 (0.1000) |
| HB ₁ | HA | " " | " " | 0.1596 (0.1458) |
| HD ₂ | HA | " " | " " | 0.1191 (0.1000) |
| HB ₂ | HA | " " | " " | 0.1596 (0.1458) |
| HO | HO | 0.000000 | 0.000000 | 0.4619 (-) |
| O ₂ | O | 0.295992 | 0.87864 | -0.5237 (-0.7282) |
| OH | OH | 0.306647 | 0.880314 | -0.6417 (-0.7282) |
| S | S | 0.356359 | 1.04600 | -0.1518 (-0.3504) |
| PET | | | | |
| CA ₁ | CA | 0.339967 | 0.359824 | 0.0298 (0.0267) |
| CA ₂ | CA | " " | " " | -0.1582 (-0.1613) |
| CA ₃ | CA | " " | " " | -0.1582 (-0.1613) |
| CA ₄ | CA | " " | " " | -0.1799 (-0.1829) |
| CA ₅ | CA | " " | " " | -0.1799 (-0.1829) |
| CA ₆ | CA | " " | " " | -0.0932 (-0.0964) |
| CT ₁ | CT | 0.339967 | 0.45773 | -0.0026 (-0.0057) |
| CT ₂ | CT | " " | " " | -0.1101 (-0.1132) |
| HT ₃ | H ₁ | 0.247135 | 0.0656888 | 0.0773 (0.0742) |
| HT ₄ | H ₁ | " " | " " | 0.0773 (0.0742) |
| HA ₂ | HA | 0.259964 | 0.06276 | 0.1468 (0.1437) |
| HA ₃ | HA | " " | " " | 0.1468 (0.1437) |
| HA ₄ | HA | " " | " " | 0.1469 (0.1438) |
| HA ₅ | HA | " " | " " | 0.1469 (0.1438) |
| HA ₆ | HA | " " | " " | 0.1287 (0.1257) |
| HT ₁ | HC | 0.264953 | 0.065888 | 0.0903 (0.0872) |
| HT ₂ | HC | " " | " " | 0.0903 (0.0872) |
| S | S | 0.356359 | 1.04600 | -0.1990 (-0.2021) |

Table 2: Bonded parameters.

| bond | k_b (kJ mol ⁻¹ nm ⁻²) | d_{eq} (nm) |
|---|--|-------------------|
| Au_{surf}–S | 62730² | 0.241 |
| Au_{lig}–S | 62730² | 0.233 |
| CA–S | 198321.6* | 0.175 |
| CT–S | 99113.0² | 0.184 |
| angle | k_θ (kJ mol ⁻¹ rad ⁻²) | θ_{eq} (°) |
| Au_{surf}–S–Au_{lig} | 460.240³ | 91.3 |
| S–Au_{lig}–S | 1460.240³ | 172.4 |
| Au_{lig}–S–Au_{lig} | 1460.240³ | 100.0/119.2 |
| Au_{surf}–S–C | 146.370² | 111.6 |
| Au_{lig}–S–C | 146.370² | 106.8 |
| CA–C–OH | 585.76* | 112.0 |
| CA–C–O | 585.76* | 126.0 |
| CA–CA–S | 418.40* | 120.0 |
| S–CT–HC | 418.40* | 107.0 |
| H₁–CT–CA | 418.40* | 109.0 |
| dihedral | (kJ/mol) | ψ |
| X-X-CA-S | 4.60240* | 180.00* |
| C-CA-CA-CA | 4.60240* | 180.00* |

Force field validation

The observation that the cluster symmetries remained intact during 100 ns of MD simulations, suggests the validity of using only a Lennard-Jones potential to describe the interactions between the gold atoms in the core of the cluster. Although gold core stability has often been considered as only criterion for the validity of the force field, we also inspected the conformational dynamics of the staples. In contrast to the dynamics of the gold atoms in the core, rather large fluctuations of the staple geometries were observed in our trajectories. In particular the V-shaped staples distort significantly with respect to the DFT optimum geometry, as illustrated in Figure 5.

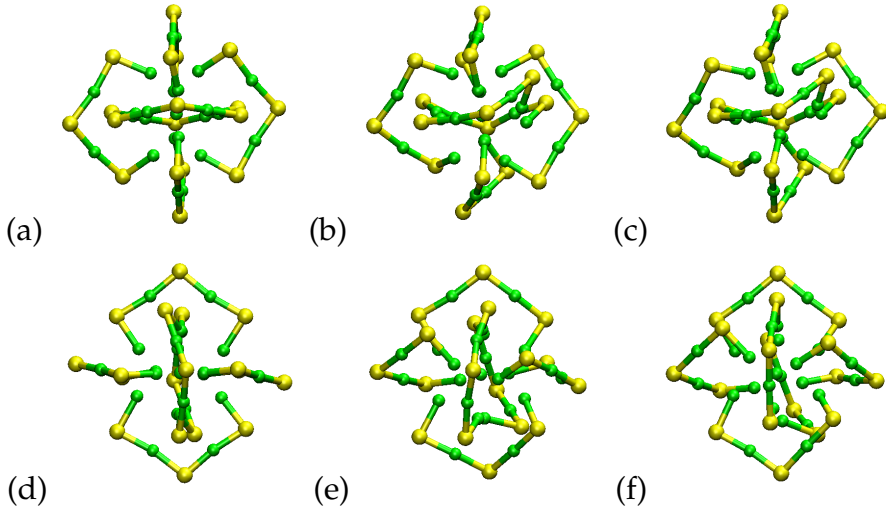


Figure 5: Staple distortion in the simulation of $\text{Au}_{25}(\text{PET})_{18}^{(-)}$. (a), (d) show the original structure; (b), (e) the structure after 100 ns simulation and (c), (f) the structure averaged from the 100 ns simulation.

From figure 5 it can be seen that there is no clear visual difference in structures after 100 ns ((b),(e)) and the one averaged over the 100 ns simulation ((c),(f)). This indicates, e.g., that folding of the top staple ((b), (c)), where the S_{surf} approaches the S_{surf} of the adjacent staple, is not continually reversed (folded back) during the simulation.

W

To verify whether the fluctuations in staple geometries are realistic, we calculated the energy profile associated with these fluctuations. In addition, we performed DFT molecular dynamics simulations and compared the staple dynamics to that observed in the force field simulations.

Potential profiles

NOTE THIS SECTION REQUIRES SOME WORK. FOR NOW PROCEED TO crystal simulations

A potential for flipping the central ligand in one, isolated staple unit of $\text{Au}_{102}(\text{pMBA})_{44}$ and $\text{Au}_{25}(\text{PET})_{18}$, were computed with DFT. For comparison, we computed the MM

energies along these pathways as well. Both profiles are shown in figure 6.

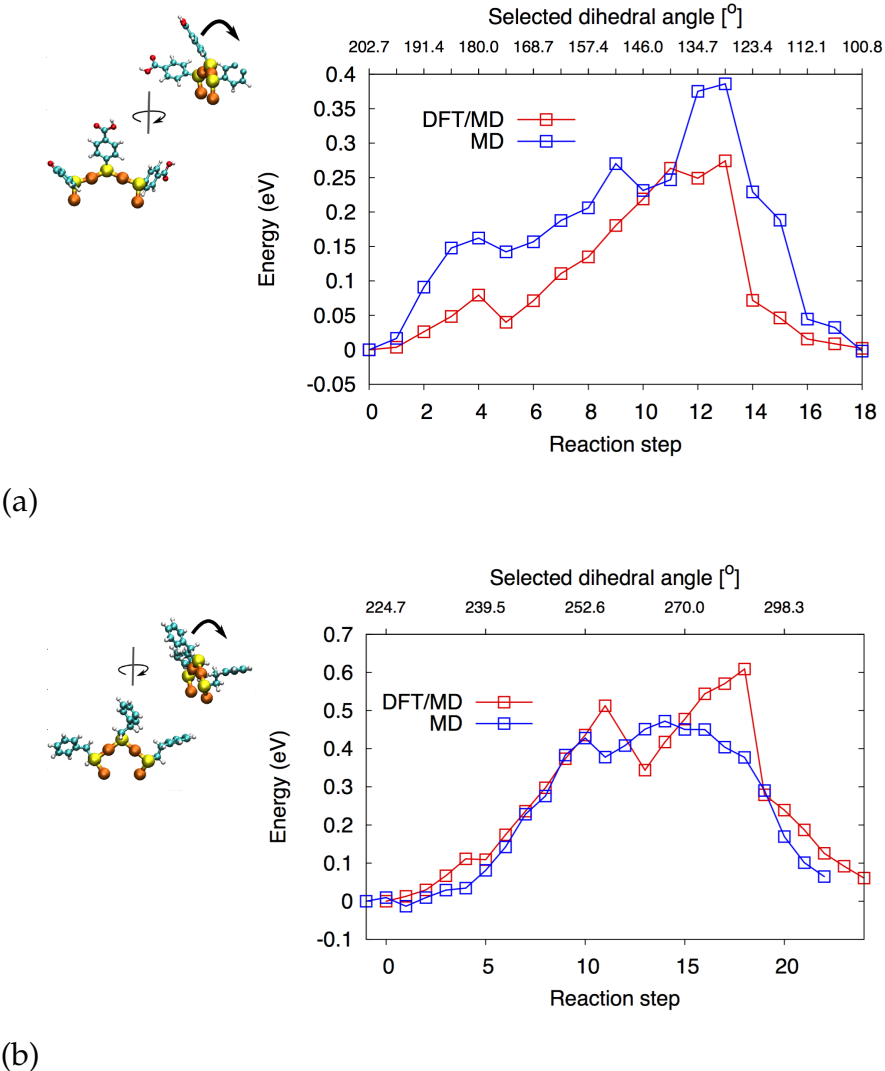


Figure 6: Ligand flipping potentials in isolated unit structures from clusters (a) Au₁₀₂, (b) Au₂₅.

Constrained relaxation DFT predicts barriers of around 0.3 eV and 0.6 eV for the central ligand flipping in the Au₁₀₂ and Au₂₅ staples, respectively. Corresponding barriers in MD are around 0.4 eV and 0.5 eV. The barriers in MD are therefore in the same order of magnitude compared to DFT. Due to the relatively low barriers, flipping in the room temperature could be expected for all these clusters.

MD/DFT simulations

NEED TO WORK ON THIS AS WELL.

The dynamics and structural fluctuations of the $\text{Au}_{25}(\text{PET})_{18}^-$ cluster were studied in picosecond time scale in vacuum with DFT/MD simulations and compared to classical MD simulations. Structural fluctuations were studied by examining distributions of atomic distances and angles in different simulations, presented in figures 7 and 8.

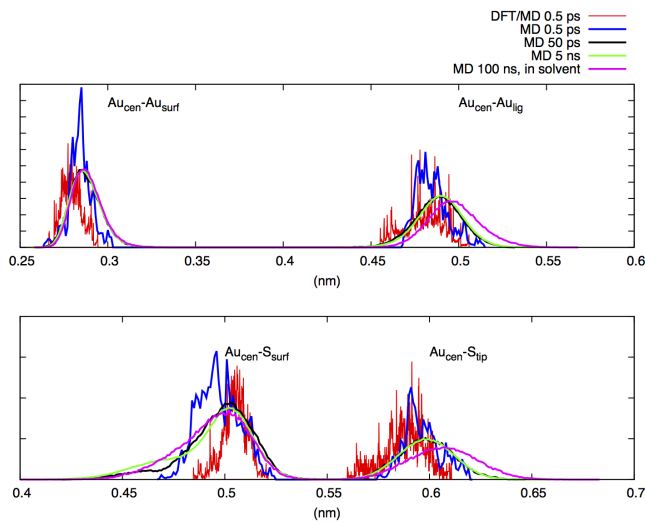


Figure 7: Distribution of atom distances from the central Au atom.

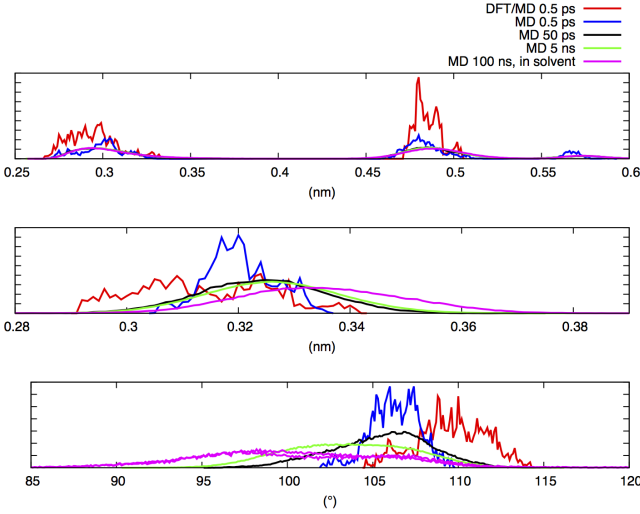


Figure 8: Bond and angle distributions.

The distributions of distances and angle generally broaden with increasing simulation time. The main difference between DFT/MD and MD is seen with shifting of averages (peak positions), also in comparing between MD simulations of different simulation times, occasionally evening out the gap between MD and DFT/MD. The differences could be due, e.g., insufficient sampling (averaging) in the short runs and differences in equilibration or thermalization between MD and DFT/MD. The clearest difference appears with the reported angle, with a decreasing trend observed in going from DFT/MD to MD. The distribution of the angle also widens with increasing simulation time.

Comparing the distance and angle distributions to longer DFT/MD simulation (10 ps) for $\text{Au}_{25}\text{H}_{18}^-$ presented in¹², there appear no drastic differences in the observed distance and angle ranges. Especially, the ranges of the reported distances and angle appearing in the longer time scale MD simulations do not exceed those observed already in 10 ps DFT/MD. Mean square displacements reported in¹² also qualitatively agree to those observed in this work for similar time scale. The peak positions or averages for bond distances qualitatively agree as well between MD and DFT/MD. The most emphasized difference appears again in the $S_{\text{surf}}-\text{S}_{\text{tip}}-S_{\text{surf}}$ angle, which on average for MD appears

clearly smaller compared to DFT/MD.

In conclusion, based on the reported distances the structural fluctuations in the cluster do not drastically differ between MD simulation compared to DFT/MD scheme. However, the 0.5 ps simulation at DFT/MD does not visually appear to caption the distortion or folding of the staples observed in the MD simulations, which could be due to insufficient sampling. This could also in part be reflected in the observed distributional difference in the $S_{\text{surf}} - S_{\text{tip}} - S_{\text{surf}}$ angle between MD and DFT/MD. In general the range of angles and distances agree between DFT/MD. In spite of the small distortions of the staples in MD the overall shape of the cluster is retained, suggesting that the intracluster interactions are sufficiently well described for the purposes of this work.

Diffusion coefficients

Diffusion coefficients for three clusters for which experimental data is available are listed in Table 3 for various box sizes. A error-weighted linear fit of the diffusion coefficient as a function of $1/L$ was extrapolated to infinite box size to correct for finite size effects. The extrapolated diffusion coefficients are listed in bold. Experimental results taken from¹⁶ are presented for comparison.

Table 3: Diffusion coefficients calculated from Einstein relation and averaged from 20 separate 5 ns simulations. Errors estimated from difference between fits of 0.5-2.5 ns and 2.5-4.5 ns. Final result in infinite box size estimated from error weighted 3 point linear fit to results for different L . Experimental diffusion coefficients¹⁶ are presented from comparison (Reported experimental standard deviation <8%)

| System | L (nm) | D_{cluster} ($10^{-5}\text{cm}^2/\text{s}$) | $D_{\text{experimental}}$ ($10^{-5}\text{cm}^2/\text{s}$) |
|------------------------------------|----------|--|---|
| $\text{Au}_{25}(\text{PET})_{18}$ | 2.32 | 0.015 ± 0.001 | |
| $\text{Au}_{25}(\text{PET})_{18}$ | 4.13 | 0.213 ± 0.02 | |
| $\text{Au}_{25}(\text{PET})_{18}$ | 6.07 | 0.367 ± 0.06 | |
| $\text{Au}_{25}(\text{PET})_{18}$ | ∞ | 0.479 ± 0.04 | 0.484 |
| $\text{Au}_{38}(\text{PET})_{24}$ | 2.55 | 0.015 ± 0.001 | |
| $\text{Au}_{38}(\text{PET})_{24}$ | 4.58 | 0.118 ± 0.04 | |
| $\text{Au}_{38}(\text{PET})_{24}$ | 6.64 | 0.287 ± 0.03 | |
| $\text{Au}_{38}(\text{PET})_{24}$ | ∞ | 0.426 ± 0.08 | 0.374 |
| $\text{Au}_{144}(\text{PET})_{60}$ | 3.46 | 0.030 ± 0.003 | |
| $\text{Au}_{144}(\text{PET})_{60}$ | 5.90 | 0.185 ± 0.002 | |
| $\text{Au}_{144}(\text{PET})_{60}$ | 8.35 | 0.252 ± 0.04 | |
| $\text{Au}_{144}(\text{PET})_{60}$ | ∞ | 0.405 ± 0.001 | 0.356 |

The experimentally observed trend that the diffusion coefficient increases with increasing cluster size is also observed in our simulations. However, the diffusion coefficients of $\text{Au}_{25}(\text{PET})_{18}$ is too small compared to experiment, whereas those of $\text{Au}_{38}(\text{PET})_{24}$ and $\text{Au}_{144}(\text{PET})_{60}$ are larger than experiment. Nevertheless, the diffusion coefficients from the simulations of the smaller nanoclusters are within the error estimates of the measured diffusion coefficients.

The discrepancies between calculated and experimental diffusion coefficients may have various origins in addition to inaccuracies in the force field. First, the convergence of the calculated diffusion coefficients is rather poor due to poor statistics. Second, the diffusion coefficient is strongly dependent on solvent viscosity. Viscosity in turn can depend on the deuteration of the solvent. In the experiments, deuterated solvents (CDCl_3 and CD_2Cl_2) were used, whereas we used parameters for the protonated solvents (CHCl_3 and CH_2Cl_2).

Despite these differences, the overall agreement between the diffusion of the cluster in

the in simulations and experiment is encouraging and suggests the hydrodynamic radius of the cluster is in line with experiment. As the hydrodynamic radius depends strongly on the fluctuations of the staples, we can also consider these fluctuations to be realistic and part of the normal thermal fluctuations of the gold clusters in solution.

Crystal simulation

As a final test for the validity of our force field parameters, we performed a 100 ns MD simulation of a crystal of $\text{Au}_{102}(\text{pMBA})_{44}$, for which the experimental x-ray structure is available. We performed simulations of 72 asymmetric units in a periodic unitcell. The empty cavities between the clusters were filled with either pure water, or a mixture of water , methanol, NaCl and NaOAc, which closely resembles the solvent used during crystallization. Whereas in simulations with water as a crystal solvent the agreement with experiment quickly deteriorates (supporting information), the crystal is stable when the mixture of solvents is used (Figure 9) The small structural deviations between the experimental structure and the averaged simulated structure seen in Figure 9 could be due to using a single protonation state of the pMBA ligands, which affects intermolecular hydrogen bonding. Alternatively, the solvent may have not been fully equilibrated during the simulation. Nevertheless, the agreement with the x-ray data further supports the view that our force field is sufficiently accurate for classical MD simulations, and we are currently performing MD simulations of various systems of gold clusters.

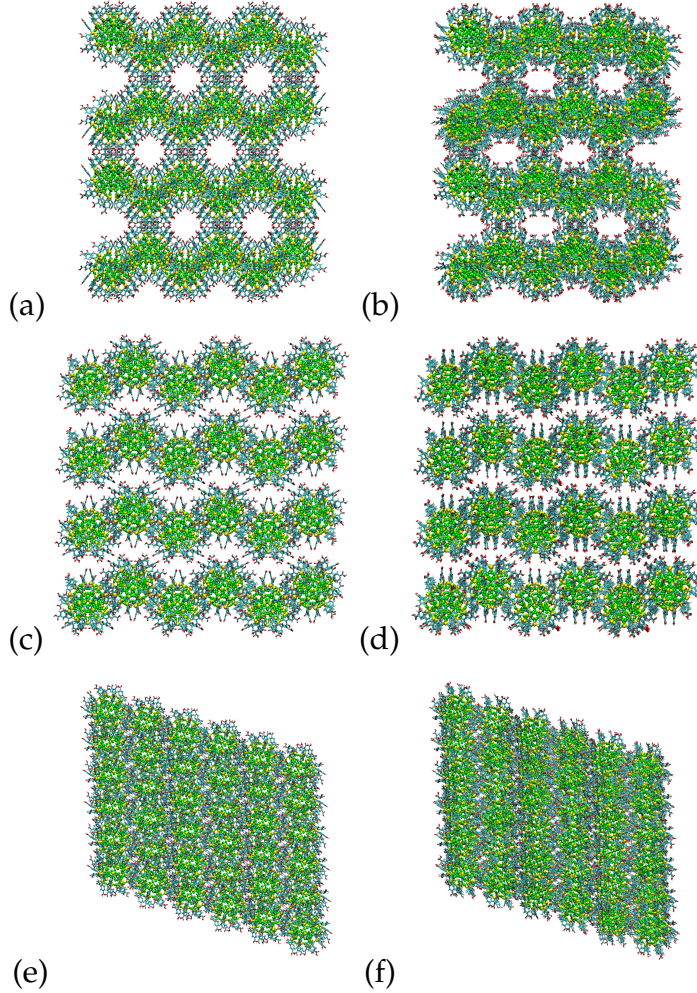


Figure 9: Simulation of 72 cluster crystal of $\text{Au}_{102}(\text{pMBA})_{44}$. (a), (c), (e) show the experimental crystal structure and (b), (d), (f) the averaged structure from 100 ns production simulation.

In the supporting information we provide the force field files with our parameters for the gromacs simulation program. The contents of these files are easily converted to other programs that support AMBER force fields.

Conclusion and outlook

We have optimized AMBER force field parameters for thio-protected gold clusters. For transferrability, we have optimized one parameter set for a wide range of clusters, rather

than multiple sets for specific clusters. Whereas the latter strategy may provide the most accurate description of the cluster that has been parameterized, the parameterization would need to be repeated for every new cluster considered, which can be time consuming. Also, geometries must be available beforehand, which precludes the use of the force field to predict the geometry of new clusters that are too large for a DFT treatment. Instead, we have optimized the parameters by considering three representative thiolate-protected gold cluster simultaneously. Furthermore, we use a non-covalent Lennard-Jones potential to describe the interactions between gold atoms in the core, which is essential for a transferrable force field.

In contrast to many previous works, we have validated our force field parameters by comparing the results of classical MD simulations of gold cluster to the results of both DFT calculations and experiment. The energetics of structural fluctuations show nice agreement to DFT data, while also experimentally determined diffusion constants and crystal structures could be reproduced with sufficient accuracy for MD simulation.

Because AMBER is a force field with parameters for a wide variety of biological compounds, including nucleic acids, proteins, sugars, and phospholipids, our work opens up the possibility to systematically investigate the effect of thiolate protected gold nanoclusters on the structure and stability of biomolecules. This is particularly relevant now that gold clusters are increasingly being used as contrast agents or molecular rulers in bio-imaging applications. Understanding the interactions between biological matter and gold clusters will also be essential for designing new strategies to conjugate these clusters with biomolecules. Atomistic simulations can provide these insights and may therefore play an essential role in driving this field forwards.

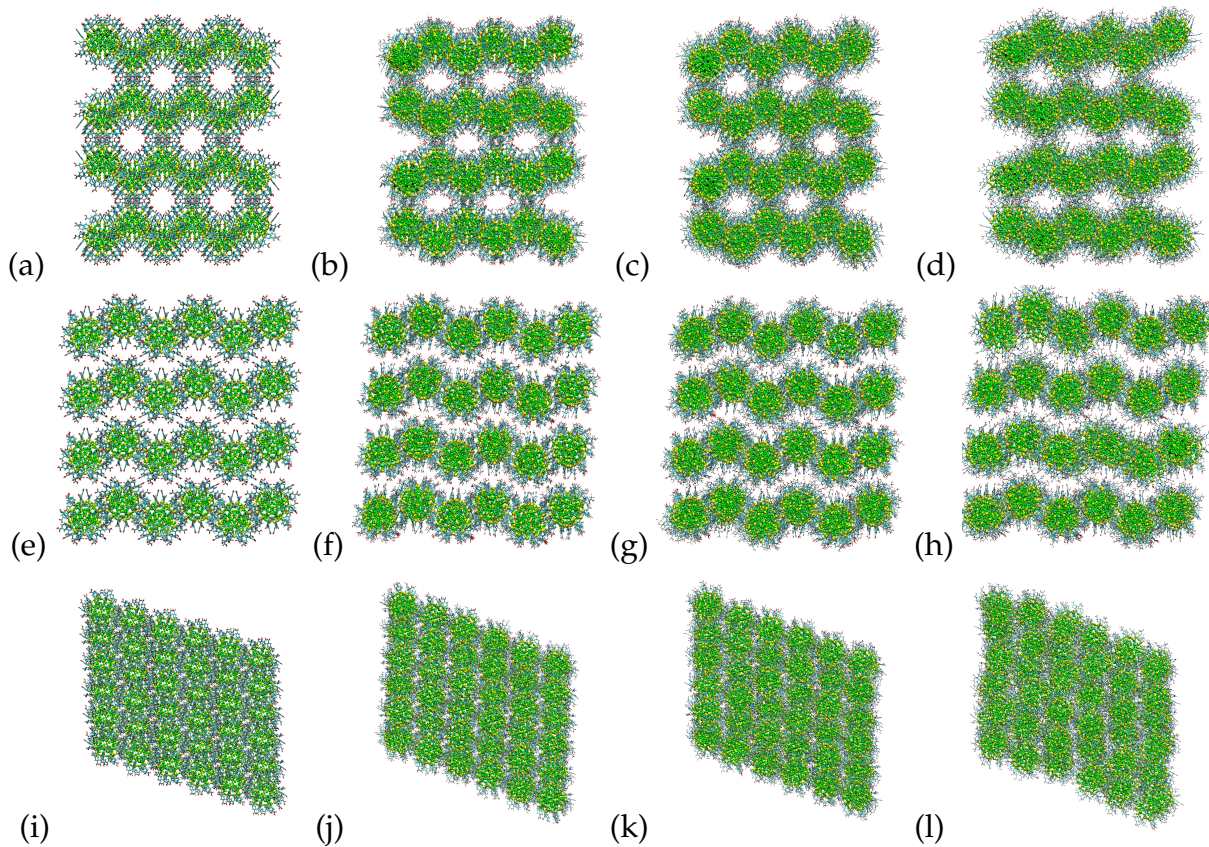


Figure S1: Simulation of 72 cluster crystal of $\text{Au}_{102}(\text{pMBA})_{44}$. (a), (e), (i) show the experimental crystal structure and (b), (f), (j) the structure in mimic solvent, (c), (g), (k) in uncompressed water, (d), (h), (l) in compressed water after 10 ns production simulation.

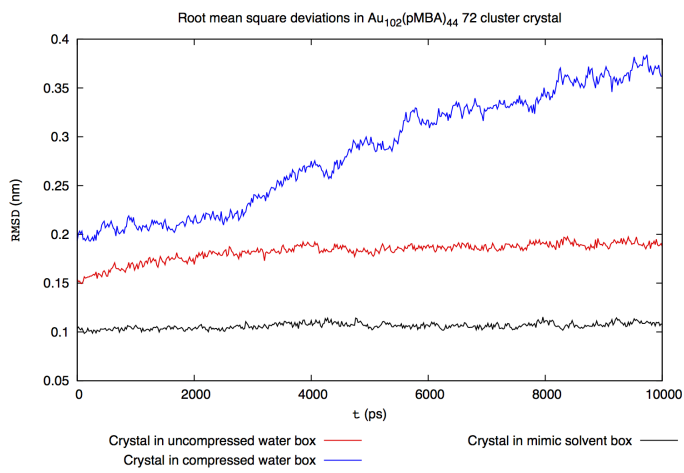


Figure S2: Root mean square deviations in crystal simulation.

References

- (1) Häkkinen, H. *Nature Chemistry* **2012**, *4*, 443–455.
- (2) Banerjee, S.; Montgomery, J.; Gascón, J. *Journal of Materials Science* **2012**, *47*, 7686–7692.
- (3) Heikkilä, E.; Gurtovenko, A. A.; Martinez-Seara, H.; Häkkinen, H.; Vattulainen, I.; Akola, J. *The Journal of Physical Chemistry C* **2012**, *116*, 9805–9815.
- (4) Case, D. A. et al. AMBER 12. 2012; <http://ambermd.org/>.
- (5) Leng, Y.; Krstić, P. S.; Wells, J. C.; Cummings, P. T.; Dean, D. J. *The Journal of Chemical Physics* **2005**, *122*, –.
- (6) Frisch, M. J. et al. Gaussian09 Revision D.01. Gaussian Inc. Wallingford CT 2009.
- (7) Weigend, F. *Phys. Chem. Chem. Phys.* **2006**, *8*, 1057–1065.
- (8) Wang, J.; Wolf, R. M.; Caldwell, J. W.; Kollman, P. A.; Case, D. A. *Journal of Computational Chemistry* **2004**, *25*, 1157–1174.
- (9) Caleman, C.; van Maaren, P. J.; Hong, M.; Hub, J. S.; Costa, L. T.; van der Spoel, D. *Journal of Chemical Theory and Computation* **2012**, *8*, 61–74, PMID: 22241968.
- (10) van der Spoel, D.; van Maaren, P. J.; Caleman, C. *Bioinformatics* **2012**, *28*, 752–753.
- (11) Enkovaara, J. et al. *Journal of Physics: Condensed Matter* **2010**, *22*, 253202.
- (12) Mäkinen, V.; Häkkinen, H. *The European Physical Journal D* **2012**, *66*.
- (13) Yeh, I.-C.; Hummer, G. *The Journal of Physical Chemistry B* **2004**, *108*, 15873–15879.
- (14) Jadzinsky, P. D.; Calero, G.; Ackerson, C. J.; Bushnell, D. A.; Kornberg, R. D. *Science* **2007**, *318*, 430–433.
- (15) Heinz, H.; Vaia, R. A.; Farmer, B. L.; Naik, R. R. *J. Phys. Chem. C* **2008**, *112*, 17281–17290.

- (16) Salorinne, K.; Lahtinen, T.; Koivisto, J.; Kalenius, E.; Nissinen, M.; Pettersson, M.; Häkkinen, H. *Analytical Chemistry* **2013**, *85*, 3489–3492, PMID: 23506040.